# Flapping Flight of Tiny Insects: Role of Bristled Wings

Vishwa Teja Kasoju, Mitchell P. Ford and Arvind Santhanakrishnan

School of Mechanical and Aerospace Engineering, Oklahoma State University Stillwater, OK 74078-5016 askrish@okstate.edu

The aerodynamics of flapping flight for the smallest insects such as thrips (body length < 1 mm) is often characterized by a 'clap and fling' of the wings at the end of the upstroke and the beginning of the downstroke. These insects fly at a Reynolds number (Re) on the order of 10 or less where viscous effects are significant. In addition, tiny flying insects show a distinctive physical adaptation in the use of bristled wings. This study examines if there are unique aerodynamic advantages associated with the use of bristled wings in clap and fling wing-wing interaction, for Re on the orders of 1-10. A robotic platform was developed for this study, in which a pair of physical wing models were programmed to execute clap and fling kinematics. Force measurements were conducted on solid (nonbristled) and bristled wing pairs. Three bristled wing models of varying bristle spacing were considered in this study. The results show lift and drag coefficients were both lowered for bristled wings when compared to solid wings for Re ranging from 1-10. Peak lift to peak drag ratio of bristled wings was observed to be larger than solid wings for this range of Re, due to disproportionally smaller reduction in lift relative to a larger decrease in drag. Particle image velocimetry (PIV) measurements conducted along the wing span show that recirculating flow through the bristles is central to the observed drag reduction.

# I. Introduction

Tiny insects of body length less than 1 mm, such as thrips, fairyflies and parasitoid wasps, are reported to fly at Reynolds number (Re) on the order of 10 or lower (Santhanakrishnan et al., 2014), and use wingwing interaction via the 'clap and fling' mechanism (Weis-Fogh, 1975; Ellington, 1980) as a part of their flight kinematics (Figure 1). In contrast to the aerodynamics of flapping flight in insects ranging from the scale of the hawk moth down to the scale of the fruit fly, the aerodynamics of flight in these small flying insects remains relatively unexplored. Several researchers (Spedding & Maxworthy, 1986; Ellington, 1984) have looked into the aerodynamics of solid/flat-plate wing models mimicking clap and fling kinematics and observed the formation of a leading edge vortex at the start of fling, which was attributed to generate lift force required to fly. However, wings of tiny insects show the presence of long bristles at the fringes that are attached to a thin solid membrane (Figure 1). Interestingly, wing bristles are not commonly observed in flight-capable insects larger than fruit flies ( $Re \sim \mathcal{O}(100)$ ). It is unclear if bristled wings are uniquely advantageous to flapping flight at Re < 100. Recent studies (Sunada et al., 2002; Santhanakrishnan et al., 2014; Jones et al., 2016) have investigated the effect of bristles on aerodynamics of flapping flight at low Re and reported predominant decrease in drag force for bristled wings as compared to solid wings. However, the effect of bristles on lift generation as well as the underlying mechanism of drag reduction by bristles have not been previously examined.

At the small scales relevant to the flight of these tiny insects (chord length  $\leq 0.5$  mm), viscous forces are dominant in comparison to inertial forces ( $Re \sim \mathcal{O}(10)$ ). Thus, we can expect a considerable increase in energetic demand needed to flap the wings in the face of increased resistive forces (drag) experienced by the wings. However, field observations in thrips (Rodriguez et al. , 2010) provide evidence of their capabilities of directed flight as well as large-scale dispersal and migration. Studies of the aerodynamics of flapping flight in tiny insects can provide us with a fundamental understanding of the physical mechanisms

Copyright  $\odot$  2018 by the authors. Published by the American Institute of Aeronautics and Astronautics, Inc. with permission.

that are responsible for sustaining force generation at these smaller scales. Understanding the coupled roles of bristled wing design and wing-wing interaction used by tiny insects can potentially aid in identifying biomimetic scaling constraints and design modifications needed for miniaturizing micro aerial vehicles.

The central hypothesis of this study is that for a wing pair performing 'clap and fling' kinematics at low Re on the orders of 1–10, both lift and drag forces will decrease for bristled wings as compared to solid wings. Further, we hypothesize that drag reduction with bristled wings will be larger in proportion to their effect on lift reduction, such that lift over drag ratio will be larger for bristled wings as compared to solid wings of equivalent geometry. A dynamically scaled robotic model was used to simulate clap and fling kinematics. Scaled-up physical models of bristled wings, varying in bristle spacing, were tested in comparison to a geometrically equivalent solid wing. Lift and drag forces were measured to quantify instantaneous and peak aerodynamic force coefficients. Chordwise and spanwise particle image velocimetry (PIV) measurements were conducted to visualize leading and trailing edge vortices as well as flow through the bristles.

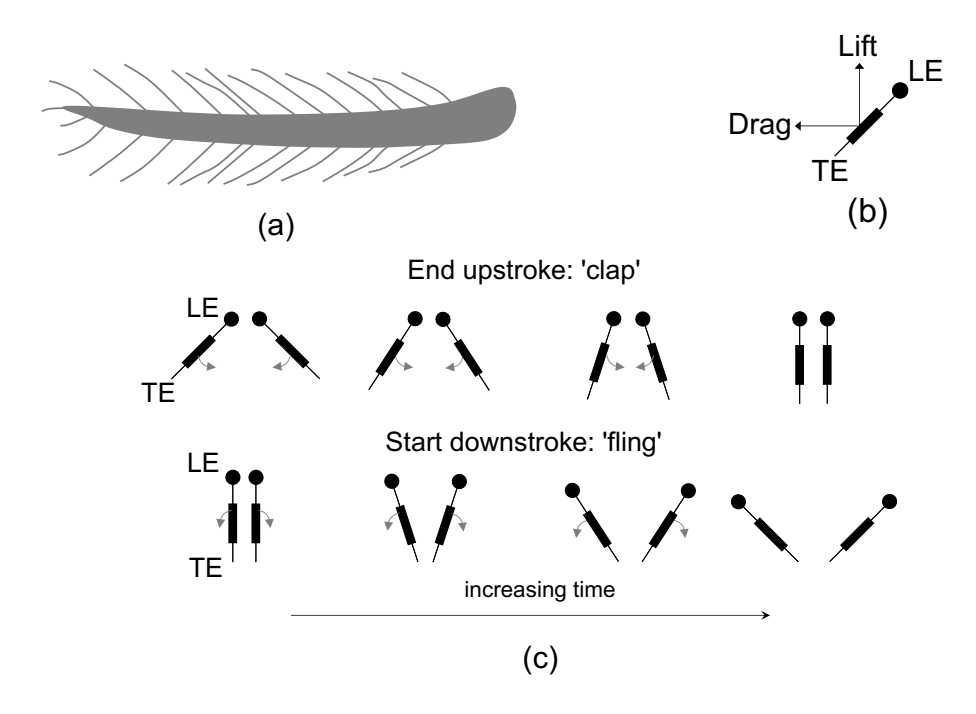


Figure 1. Clap and fling interaction in tiny insects with bristled wings. (a) Representative bristled wing of thrips (Euphysothrips, redrawn from Mound & Ng, 2009); (b) transverse cross-section of a bristled wing showing chordwise view and directions of lift (vertical) and drag (horizontal) forces examined in this study; and (c) chordwise view of the wings during clap (top) and fling (bottom). At the end of the upstroke, a pair of wings rotate about their leading edges and come in close proximity. At the beginning of down stroke, the wings rotate with respect to trailing edges and fling them apart. LE = leading edge; TE=trailing edge.

# II. Experimental Arrangements

#### A. Robotic Model

The model used for replicating 'clap and fling' wing-wing interaction (Figure 2) consists of two wings that were programmed to move symmetrically in opposite directions. Translation and rotation of each wing was achieved using two programmable 2-phase hybrid stepper motors with integrated encoders (model ST234E, National Instruments Corporation, Austin, TX). Each pair of rotational and translational stepper motors were rigidly mounted onto an aluminum base plate, which in turn was allowed to slide with minimal friction within two T-slotted extrusions using bearing pads. Each wing was mounted onto a stainless steel D-profile shaft of diameter  $6.35 \times 10^{-3}$  m via a custom-made aluminum L-bracket (Figure 2). Each D-profile shaft was coupled to one rotational stepper motor using a pair of nylon miter gears for transmitting motion from the rotational stepper motor shaft at a 90-degree angle. Each translational stepper motor was coupled to a nylon pinion gear that was in turn coupled to a 0.30 m long nylon rack. The rack for each translational stepper motor was rigidly mounted onto an aluminum bar that was coupled to the T-slotted extrusion. Each

of the two D-profile shafts passed through the aluminum base plate and was supported by a steel ball bearing that was press-fitted onto the aluminum base plate. All the stepper motors were controlled using a multi-axis motion controller (PCI -7350, National Instruments Corporation, Austin, TX) via a custom program in LabVIEW software (National Instruments Corporation, Austin, TX). One revolution of each stepper motor was divided into 20,000 steps using a stepper motor drive (model SMD-7611, National Instruments Corporation, Austin, TX). The entire assembly was mounted on the top of a  $10.6 \times 10^{-2}$  m<sup>3</sup> acrylic tank. The tank had a square cross-section of 0.51 m $\times 0.51$  m and was 0.41 m tall. The working fluid used was 99% glycerin, such that the wings were completely immersed in the fluid.

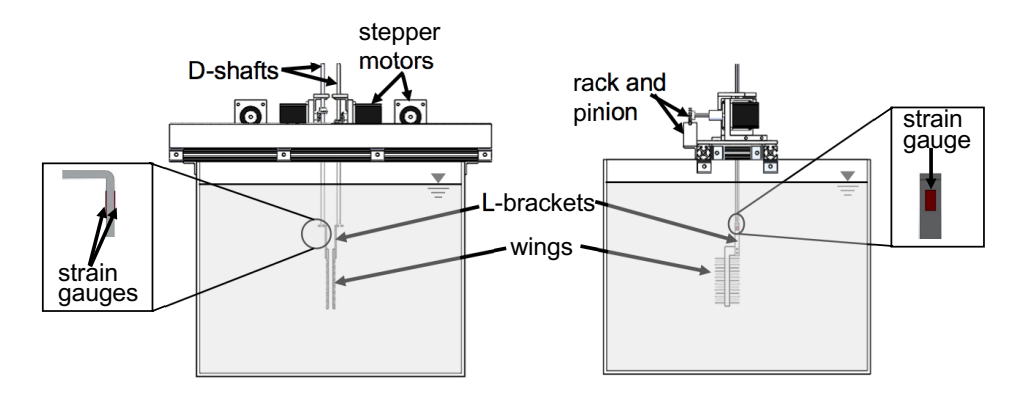


Figure 2. Schematic diagram of experimental setup: front view (left) and right side view (right).

## B. Physical Models

Physical models of solid and bristled wings were fabricated using a  $3.17 \times 10^{-3}$  m thick polycarbonate sheet, such that the model wings had a rectangular cross section with  $90 \times 10^{-3}$  m span and  $45 \times 10^{-3}$  m chord (Figure 3). Our model wings were thus nearly two orders of magnitude larger than the typical length scales of tiny insect wings. Bristled wings were fabricated using a  $3.17 \times 10^{-3}$  m thick polycarbonate membrane (width  $S = 8.5 \times 10^{-3}$  m; span=  $90 \times 10^{-3}$  m) that was surrounded on either side by cylindrical glass rods of  $1.00 \times 10^{-3}$  m in diameter to represent bristles. The chord length for bristled wings are measured from one bristle tip to the opposing bristle tip on the other side of the solid acrylic membrane (Figure 3). The wing models were tested using the dynamically scaled clap and fling robotic platform for measurements of aerodynamic forces and visualization of flow structures. We tested three different bristled wing designs, in addition to a solid wing of identical chord and span. The bristled wing models tested varied in terms of the gap or spacing between a pair of bristles (G), represented here non-dimensionally using the ratio of spacing to bristle diameter (D). Figure 3 shows the solid wing and three bristled wing models that were considered in this study (G/D = 5, 11, 17). To facilitate comparison between wing designs, the number of bristles on the bristled wing models were varied while maintain the chord and span of the wing constant. Chord and span lengths were selected to reduce flow artifacts due to the confining tank walls.

## C. Kinematics

Our focus in this study was to quantify forces and flow structures during 'clap and fling' wing-wing interaction. As a result, we did not consider the flapping translation and stroke reversal portions of wing kinematics seen in the flapping flight of insects (Sane, 2003). We used the kinematics examined in a 2D computational study on clap and fling mechanism by Miller & Peskin (2005) to develop motion profiles for the stepper motors in the robotic platform. The motion profile for the stepper motors (velocity in terms of steps/second) was obtained from the variation of non dimensional velocity with non-dimensional time during clap and fling phases (Figure 4). The sinusoidal curve represents the rotational motion of one wing while the trapezoidal curve represents the translational motion of one wing. The motion profiles for the 2nd wing was made identical to the first wing, but the motion was set in opposite directional sense with respect to the 1st wing. Figure 3 shows overlap in translational and rotational motion during both clap and fling phases. During the clap phase, the wings were made to translate along with rotational motion (100% overlap) while during fling phase the wings start to translate after 50% of fling time (50% overlap). The maximum angle of rotation for

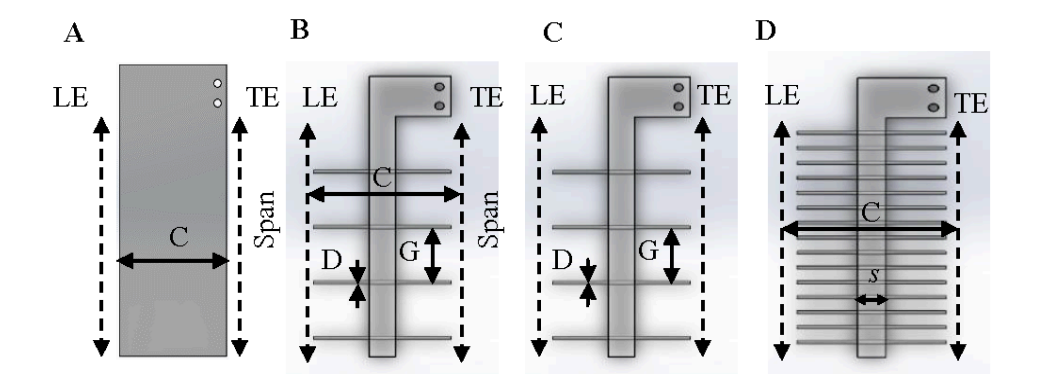


Figure 3. Physical wing models tested, shown in terms of increasing gap to diameter (G/D) ratio: (A) solid (G/D=0), B) G/D=5, C) G/D=11, D) G/D=17. Here G represents the gap between a pair of bristles, s denotes the width of solid membrane, and D is the bristle diameter. s=8.5 mm and D=1 mm for all bristled wing models. Wing span S and chord C were maintained identical between solid and bristled wing models. For the solid wing, G and D were both 0 mm, and S=C.

both clap and fling was  $45^{\circ}$ . The full set of equations used to describe translation and rotation as shown in Figure 3 can be found in Miller & Peskin (2005).

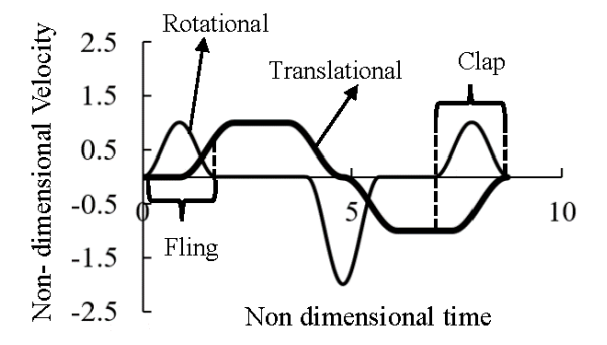


Figure 4. Prescribed wing kinematics shown as a plot of non-dimensional velocity versus non-dimensional stroke time, based on Miller & Peskin (2005). Thicker line indicates translational motion (trapezoidal profile) while the thin line indicates rotational motion of the wing.

## D. Force Measurements

Time varying forces on the wings were measured using uni-axial linear strain gauges of grid size 3.2 mm×2.50 mm and nominal resistance of 350 ohms (model SGD-3/350-LY13, Omega Engineering, Inc., Norwalk, CT). Wings were attached to the D-shaft of the robotic model (Figure 2). Two different custom aluminum L-brackets were fabricated for individual/non-simultaneous lift and drag force measurements (Figure 2). The thickness of the L-brackets used for drag and lift force measurements were  $2 \times 10^{-3}$  m and  $1 \times 10^{-3}$  m, respectively. The variation in thicknesses was necessary to resolve the lower values of lift force (in comparison to drag force) expected for low Re in the range of 5-15. Strain gauges were mounted on both sides of the L-brackets. The surfaces of the L-brackets were smoothened and cleaned thoroughly so that the strain gauges could be bonded to surfaces with minimal/negligible air gap. Though a model wing pair was driven to mimic 'clap and fling' wing-wing interaction (Figure 4), lift and drag forces were measured only on one wing of the pair. This was based on the assumption that lift and drag forces would be identical in magnitude in each wing of the wing pair, as the motion profile used for prescribing motion of both wings was symmetric.

#### Data Acquisition

Raw data in the form of analog voltage outputs were acquired using a data acquisition board (model NI USB-6210, National Instruments Corporation, Austin, TX) via a custom acquisition program written in LabVIEW software (National Instruments Corporation, Austin, TX). The strain gauge data was acquired

at a sampling frequency  $(f_s)$  of 100 kHz at all Re (5 to 15) across all the wing models (solid wing; bristled wings of G/D =5,11,17). Table 1 shows total clap and fling times during a cycle for varying Re ranging from 5 to 15. The number of samples collected during each cycle for a particular Re can be determined as the product of  $f_s$  and either fling duration or clap duration.

Re	$v_{ m max,tip}$	Clap/Fling time	$f_{ m cut ext{-}off}$	$f_{\mathrm{TR-PIV}}$	$f_{ m PL-PIV}$
	[cm/s]	[ms]	[Hz]	[frames/s]	[image pairs/s]
5	9.1	860	12	116	0.12
8	14.6	540	19	185	0.19
10	18.2	430	23	233	0.23
12	21.9	360	28	278	0.28
15	27.4	290	35	345	0.35

Table 1. Experimental conditions used for PIV and force measurements. Non-dimensional motion profile (Figure 4) was rescaled using either clap or fling duration. Cut-off frequency used for filtering strain gauge data ( $f_{\text{cut-off}}$ ) was varied for every Re. Camera frame rates used for TR-PIV measurements in chordwise plane ( $f_{\text{TR-PIV}}$ ) and PL-PIV measurements in spanwise plane ( $f_{\text{PL-PIV}}$ ) were varied to obtain data at identical non-dimensional times (in terms of % clap or fling). Note that  $v_{\text{max,tip}} = \text{maximum translational velocity at wing tip; Reynolds number, } Re = (v_{\text{max,tip}}C)/\nu$ . TR-PIV=time-resolved PIV; PL-PIV=phase-locked PIV.

Strain gauge data was acquired through the entire clap or fling time for each cycle. The model was run continuously for 10 clap and fling cycles prior to data collection, so as to generate a periodic steady state in the tank. Strain gauge data were collected during clap and fling across continuous cycles. Strain gauge data needed for calculation of lift and drag forces were obtained non-simultaneously (viz., one force component at a time). Further, since every wing pair tested was driven in a continuous manner (effective 'wingbeat' included both clap and fling), strain gauge data for each force component were acquired continuously for 30 cycles of clap and fling. Later, depending upon the clap and fling time (Table 1), we separated the data for clap and fling from each data set of 30 cycles. For every set of strain gauge data, we also recorded the angular position of the wing using the integrated encoders housed within the programmable 2- phase hybrid stepper motors. For every set of strain data, we also recorded the voltage signal before the start of wing motion for baseline shift/offset correction purposes.

# Processing

Raw force signals in terms of voltage were processed using a custom script written in MATLAB (The Mathworks, Inc., Natick, MA). The first step in processing was filtering the raw voltage data using a zero-phase delay, third order, low-pass digital Butterworth filter with cutoff frequency varying from 12-35 Hz. The cutoff frequency for a particular Re was approximately 10 times of the sampling frequency ( $f_s$ ) for that specific Re, the rationale for which was based on a previous study (Birch  $et\ al.$ , 2004). Table 1 presents the cutoff frequencies used for filtering at every Re in both clap and fling. The second step in processing was cycle-averaging the filtered raw force and angle data across the acquired 30 cycles each of clap and fling, and removing the zero offset by subtracting filtered zero force data from filtered non-zero force data. The third step in processing was to apply the slope obtained from strain gauge calibration to convert the filtered force signal from Volts to Newtons. The final step after applying calibration was to calculate non-dimensional coefficients of lift  $(C_L)$  and drag  $(C_D)$ .

#### E. Particle Image Velocimetry (PIV)

PIV was used to visualize the flow structures formed along the chordwise (horizontal plane) and spanwise (vertical plane) directions during the wing motion. Chordwise flow field data were used to determine the strength (circulation) of the leading edge vortex (LEV) and trailing edge vortex (TEV). Spanwise flow visualization data were used to visualize flow in between the bristles.

### PIV along chordwise direction

2D time-resolved PIV (TR-PIV) was used to visualize chordwise flow field generated during clap and fling motion of each wing pair at a particular Re (Figure 5). Hollow glass spheres of 10 microns diameter were

used as seeding particles in the fluid medium. Seeding particles were mixed in the fluid medium contained in the aquarium tank at least a day before PIV data acquisition to provide adequate time for settling and homogenous initial distribution. One horizontal PIV plane (HP at half the span of the wing) was illuminated using a single cavity Nd:YLF laser (Photonics Industry Inc., NY, USA) that provides a 0.5 mm diameter beam of 527 nm in wavelength. A cylindrical lens (10 mm focal length) was used to make a planar laser sheet from the laser beam. A high-speed 1 MP CMOS camera (Phantom Miro 110, Vision Research Inc., Wayne, NJ, USA) was positioned at the bottom of the tank and focused onto the seeding particles in the plane HP using a 60 mm constant focal length lens (Nikon Micro Nikkor, Nikon Corporation, Tokyo, Japan). The aperture of the camera lens was set to 2.8 for all experiments. A trigger signal was generated using a custom LabVIEW program at the beginning of clap and fling phases and was provided as an input to the high speed controller unit of the PIV hardware. This trigger enabled the acquisition of PIV data from the same starting point for N cycles each of clap and fling (PIV data for each phase was acquired separately). The PIV particle size was in the range of 1.5-3 pixels. Average particle displacements in the test volume ranged between 4-7 pixels, depending on Rec. PIV data were acquired for both clap and fling phases across all the conditions tested (varying Rec and wing model design). For each experiment, 100 raw PIV images per cycle (of either clap or fling) were recorded under varying frame rate based on Re (see Table 1). 10 cycles each of clap and fling were recorded separately for each experimental condition.

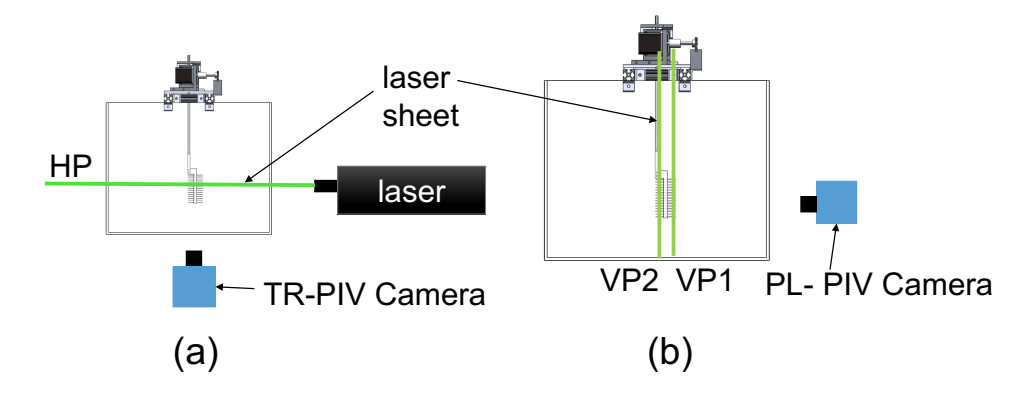


Figure 5. Schematic diagrams showing PIV setup for flow visualization along: (a) chordwise plane illuminated by laser sheet HP; (b) 2 spanwise planes illuminated by laser sheets VP1 and VP2.

#### PIV along spanwise direction

2D phase locked particle image velocimetry (PL-PIV) was used to visualize flow through the bristles of all the bristled wing models (Figure 5). Hollow glass spheres of 8-10  $\mu$ m diameter were used as seeding particles in the fluid medium. Two vertical PIV planes (VP1 and VP2 in Figure 5) were setup. VP1 was located at approximately 10% of chord length away from the leading edge and VP2 was located at approximately 10% of chord length away from the trailing edge. Each vertical PIV plane was illuminated using a double-pulsed, single-cavity Nd:YAG laser (Gemini 200-15, New Wave Research, Fremont, CA) with wavelength 532 nm, maximum repetition rate of 15 Hz and pulse width in the range of 3-5 ns. The laser beam was converted to a 2D planar sheet of thickness 5–6 mm using a cylindrical lens (10mm focal length). An sCMOS camera of spatial resolution 2600 x 2200 pixels, maximum frame rate of 100 fps, and a maximum pixel size of 6.5  $\mu$ m x 6.5 µm (LaVision Inc., Ypsilanti, MI) was used for recording raw PL-PIV image pairs in frame-straddling mode. Seeding particles in the laser sheet plane were focused using a 60 mm constant focal length lens (Nikon Micro Nikor, Nikon Corporation, Tokyo, Japan). The aperture of camera lens was set to 2.8 for all PL-PIV measurements. A trigger signal was generated for PL-PIV at the beginning of clap and fling phases (using a custom LabVIEW program) and provided as an input to the programmable timing unit (PTU) of the PIV hardware. The trigger signal was used as a reference to offset PIV image acquisition to occur at selected phase-locked time points for 10 cycles each during clap and fling phases. The PIV particle size was in the range of 1.5-3 pixels. PL-PIV data were collected at 16 different time points defined in terms of percentage of clap or fling cycle duration (fling: 30%, 35%, 45%, 50%, 55%, 65%, 70%, 100% approximately; clap: 0%,30%, 35%, 45%, 50%, 55%, 65%,70% approximately). These time points were selected based on distributing the maximum fling/clap angle into 8 equally spaced angular points (fling angles: 12.5%, 25%, 37.5%, 50%, 62.5%, 75%, 87.5%, 100%; clap angles: 0%, 12.5%, 25%, 37.5%, 50%, 62.5%, 75%, 87.5%). We used a rotating turn table with 8 equally spaced angular points drilled precisely using milling machines to collect PIV data along span wise direction of the wing at each specified angle. For every test condition (Re/clap/fling/wing design), a set of 10 image pairs (1 image pair per cycle) were acquired, phase-locked at one time point in clap/fling rotational cycle. Laser pulse separation intervals between the two images in an image pair (dt) was in the range of 2–9 ms depending on Re. Particle displacements within the FOV ranged between 4-7 pixels.

## Post processing

Raw data from chordwise and spanwise PIV recordings were processed using DaVis 8.3.0 software (LaVision GmbH, Göttingen, Germany). No pre-processing of raw PIV images were performed. Multi-pass cross-correlation was performed on the PIV image pairs with an initial window size of 64x64 pixels (2 passes) and a final window size of 32x32 pixels (2 passes), each with 50% overlap. Post-processing was performed by rejecting velocity vectors with peak ratio Q less than 1.2 and interpolation was used to replace empty vectors. The processed velocity vector fields were phase-averaged for 10 cycles of clap/fling. 2D velocity components (u in x-direction and v in y-direction) of flow in the field of view were obtained following cycle-averaging.

# III. Results

#### A. Force Coefficients

Figures 6–7 show the Re variation of maximum drag coefficient  $(C_{D,max})$ , maximum lift coefficient  $(C_{L,max})$  and ratio of peak lift over peak drag  $(C_{L,max}/C_{D,max})$  for solid and bristled wing models during clap and fling phases. In general, both  $C_{D,max}$  and  $C_{L,max}$  decreased with increasing Re for any wing model, and the decrease in force coefficients was larger for solid wings when compared to any of the bristled wings during both clap and fling phases.

For a particular Re in the range of 5 to 15,  $C_{D,max}$  and  $C_{L,max}$  decreased for the bristled wing when compared to the solid wing, irrespective of clap or fling phase. Also, the decrease in  $C_{D,max}$  in the bristled wing model was more compared to decrease in  $C_{L,max}$ . Consequently, the ratio of maximum lift coefficient to maximum drag coefficient ( $C_{L,max}/C_{D,max}$ ) was largest in the bristled wing model across all Re tested during both clap and fling times. Interestingly,  $C_{D,max}$  was observed to be nearly invariant with Re for bristled wing of largest G/D during both clap and fling phases, showing the importance of bristles in maintaining a relatively constant drag force across two orders of magnitude of Re.

With increasing G/D at a particular Re,  $C_{D,max}$  decreased while  $C_{L,max}$  was found to have little effect during both clap and fling. Hence, peak lift over peak drag  $(C_{L,max}/C_{D,max})$  increased with increase in G/D during both clap and fling.

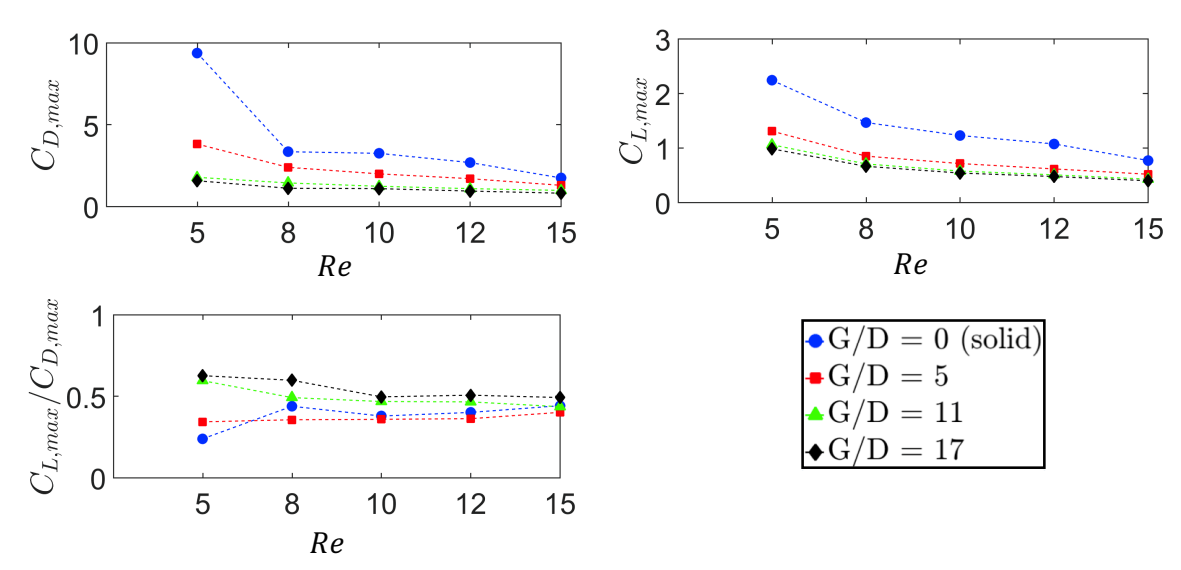


Figure 6. Force coefficients in clap phase as a function of Re and wing design. Peak drag and lift coefficients are shown in the top, while the ratio of peak lift to peak drag is shown in the bottom.

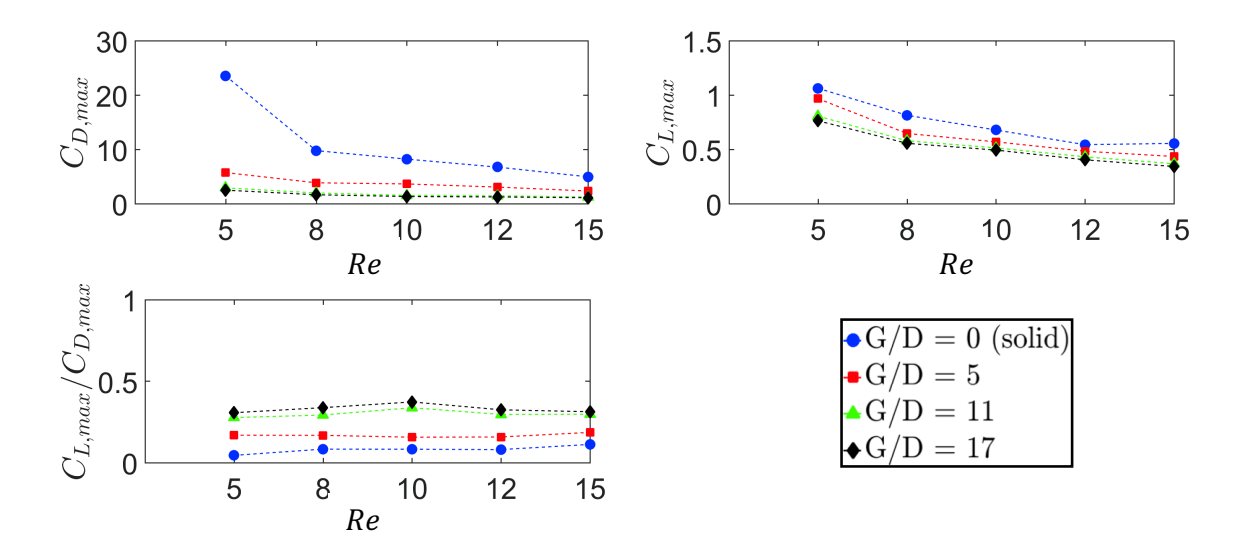


Figure 7. Force coefficients in fling phase as a function of Re and wing design. Peak drag and lift coefficients are shown in the top, while the ratio of peak lift to peak drag is shown in the bottom.

#### B. Chordwise Flow: LEV and TEV Circulation

Figures 8–11 show the out-of-plane vorticity (z) contours overlaid on velocity vector fields at Re = 10 for solid and bristled (G/D = 17) wing models at 4 time points each of clap and fling (25%, 50%, 75%, 100% of fling angle; 0%, 25%, 50%, 75% of clap angle). These were obtained from 2D TR-PIV measurements acquired at chordwise plane HP (located at mid-span, see Figure 5). During clap phase, we observed the formation of stronger TEV compared to the LEV for both the solid and bristled wing models at all time points (Figures 8–9). With increasing fling angle (Figures 10–11), we observed the formation of stronger leading edge vortex compared to trailing edge vortex at all time points for both wing models (solid, bristled). In general, both the LEV and TEV were weaker for the bristled wing when compared to those of the solid wing during clap and fling phases. The velocity vectors for bristled wing model were smaller compared to solid wing model at Re = 10 during clap and fling phases.

Since the forces generated by the wings are related to the strength of the LEV and TEV, we calculated circulation of LEV ( $\Gamma_{LEV}$ ) and TEV ( $\Gamma_{TEV}$ ) on one wing of the wing pair, by integrating out-of-plane z-vorticity ( $\omega_y$ ) from 2D TR-PIV data as:

$$\Gamma = \int_{A_v} \omega_y \ dA_v = \sum_{A_v} (\omega_y \ dx \ dz) \tag{1}$$

where  $A_v$  denotes the area enclosed by a vortex. The swirling strength criterion ( $\lambda_{ci}$ ) was used for vortex identification with a 4.2% threshold of the maximum value (Zhou et al., 1999). It is important to note that the swirling strength criterion was evaluated for turbulent flows by Zhou et al. (1999). However, we used this criterion for vortex identification in a laminar flow. This may present discrepancies between the 'true' location of the vortex (as opposed to what was identified using  $\lambda_{ci}$ ) that will need to be investigated in future studies. One of the challenges we encountered in circulation analysis, especially in the case of bristled wing models, was in distinguishing the vortex boundary when it was highly diffuse (figures 9 and 11). From the circulation analysis (figures 12 and 13),  $\Gamma_{TEV}$  was larger in clap for solid wing compared to bristled wing model, while  $\Gamma_{LEV}$  showed little change between solid and bristled wings (Figure 12). Further, both  $\Gamma_{LEV}$  and  $\Gamma_{TEV}$  do not appreciably change in the bristled wing model throughout the entire clap cycle at Re = 10. This was consistent with other Re tested (not shown). The net circulation ( $\Gamma_{Net}$ ) over the wing was calculated as the difference in circulation of LEV and TEV:

$$\Gamma_{Net} = |\Gamma_{LEV}| - |\Gamma_{TEV}| \tag{2}$$

 $\Gamma_{Net}$  in clap was larger for solid wing compared to bristled wing model (Figure 12). During fling,  $\Gamma_{LEV}$  was larger for the solid wing compared to bristled wing, while  $\Gamma_{TEV}$  did not appreciably change between solid and bristled wing models (Figure 13). For the bristled wing model, there was little change in  $\Gamma_{LEV}$  and

 $\Gamma_{TEV}$  throughout the fling cycle at Re = 10. This was also observed for all other Re tested (not shown). Finally, the net circulation ( $\Gamma_{Net}$ ) was larger for the solid wing compared to the bristled wing model.

During clap phase,  $\Gamma_{LEV}$  does not change with increase in G/D (Figure 12). However,  $\Gamma_{TEV}$  decreased with increasing G/D. For any bristled wing model (G/D=5,11,17) we did not see appreciable change in  $\Gamma_{LEV}$  throughout the entire clap at Re=10, while  $\Gamma_{TEV}$  was observed to decrease with increase in G/D. Therefore net circulation  $(\Gamma_{Net})$  was observed to decrease from solid to any bristled wing model. Also,  $\Gamma_{Net}$  for bristled wing models (G/D=5,11,17) was found to to decrease with increase in G/D.

While the drop in  $\Gamma_{LEV}$  in fling was largest between the solid and any bristled wing model,  $\Gamma_{LEV}$  was observed to be in close range for all the bristled wing models (G/D=5,11,17). However,  $\Gamma_{TEV}$  did not appreciably change with increase in G/D (Figure 13). For any bristled wing model (G/D=5,11,17) we did not see appreciable change in  $\Gamma_{LEV}$  throughout the entire fling at Re=10. Therefore net circulation  $(\Gamma_{Net})$  in fling was observed to decrease the most from solid to any bristled wing model.  $\Gamma_{Net}$  for all bristled wing models (G/D=5,11,17) was found to fall in roughly the same range.

In general, augmenting the net circulation over the wing can be beneficial to lift production. However, it is unclear if circulation-based lift may be as effective at low Re ( $O \sim 10$ ) as compared to higher Re. On this question, Ellington (1975) mentioned that Encarsia formosa used circulatory lift mechanism with a horizontal stroke plane. Therefore, a decrease in  $\Gamma_{Net}$  could contribute to a decrease in  $C_L$ . Hence, when moving from a solid to a bristled wing,  $C_L$  would decrease during both clap and fling. During fling, lift force is thus not expected to change much with increasing G/D (Figure 13). This is also supported by lift coefficient  $C_L$  variation with G/D during fling (Figure 7). During clap, the net circulation ( $\Gamma_{Net}$ ) was found to decrease with increase in G/D as compared to fling. Hence, lift force generated in clap is expected to decrease with increase in G/D.

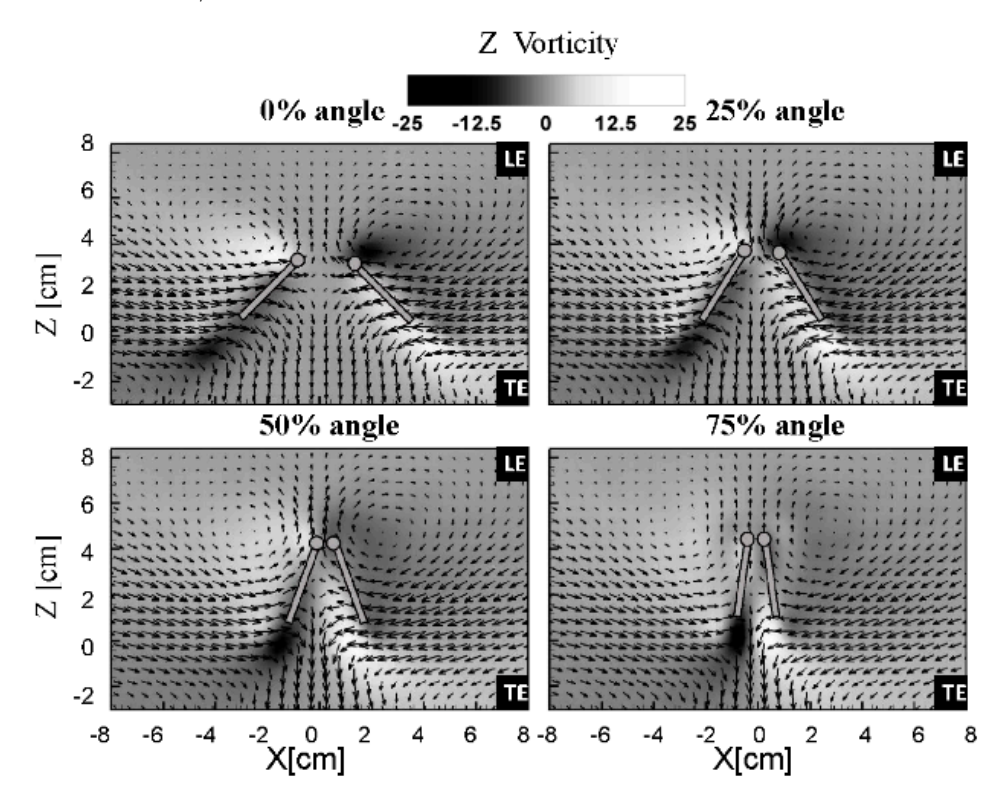


Figure 8. Out-of-plane vorticity contours overlaid with velocity vectors for solid wing model during clap at Re = 10.

#### C. Spanwise Flow

In order to generate an understanding of how the flow structures look like along the spanwise direction, we examined velocity vector fields from spanwise PIV (Figures 14–15). During fling, we observed the formation of small-scale vortices around the bristles (Figure 14). These vortices appeared to increase in size with increasing fling time until about 40% of fling duration. These small-scale vortices were also observed for

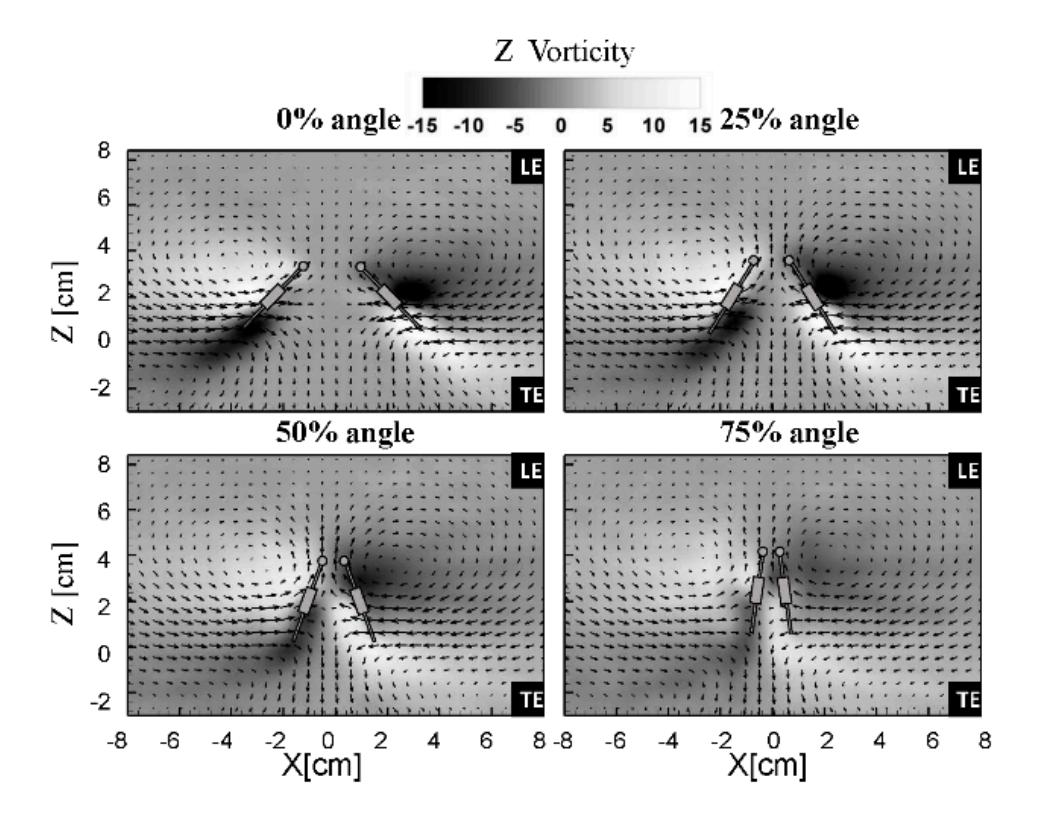


Figure 9. Out-of-plane vorticity contours overlaid with velocity vectors for bristled wing model (G/D=17) during clap at Re=10.

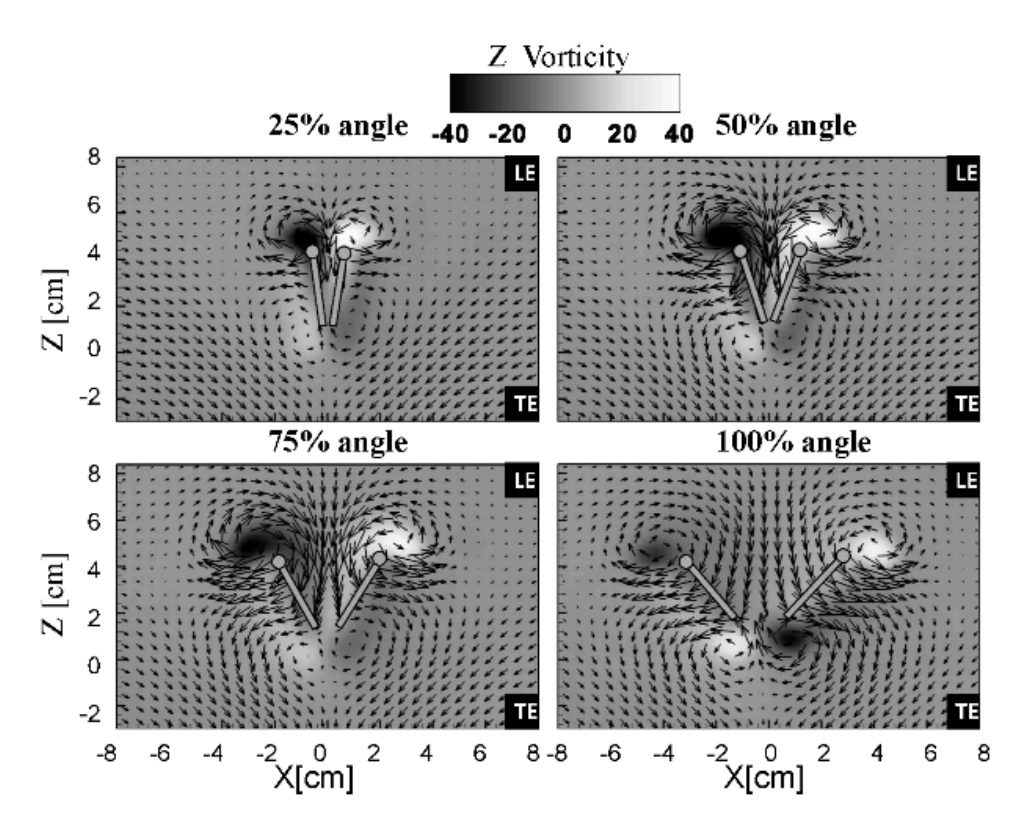


Figure 10. Out-of-plane vorticity contours overlaid with velocity vectors for solid wing model during fling at Re=10.

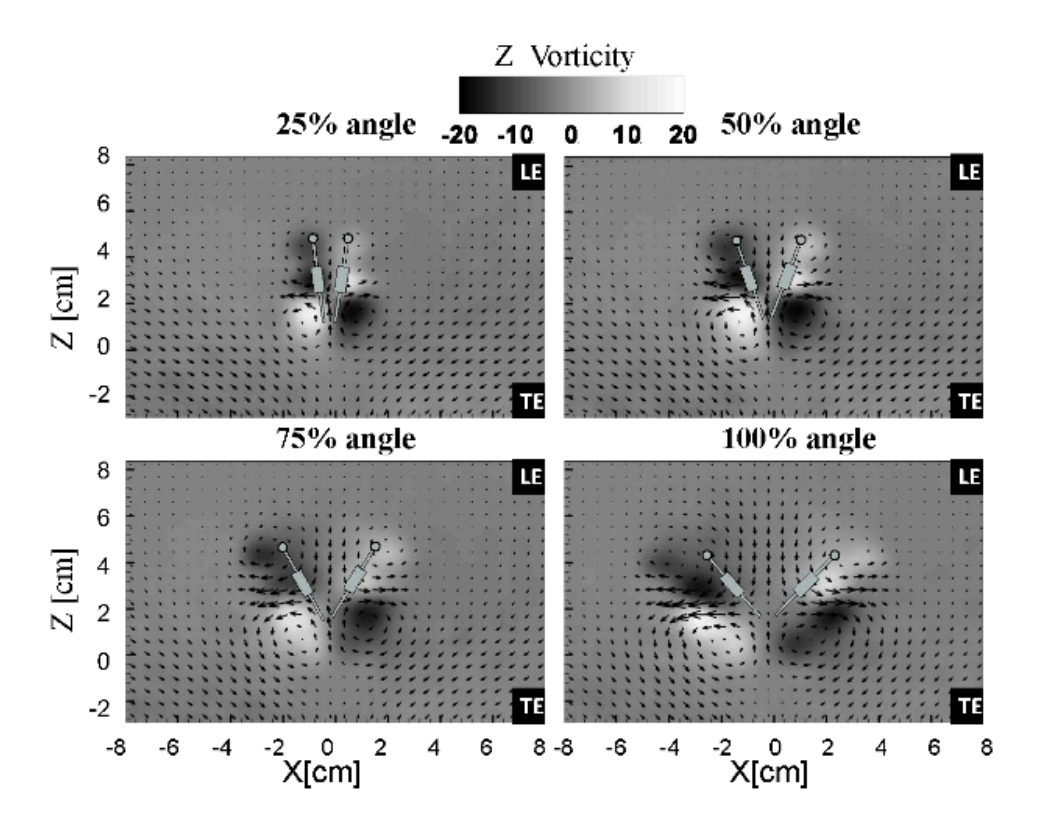


Figure 11. Out-of-plane vorticity contours overlaid with velocity vectors for bristled wing model (G/D = 17) during fling at Re = 10.

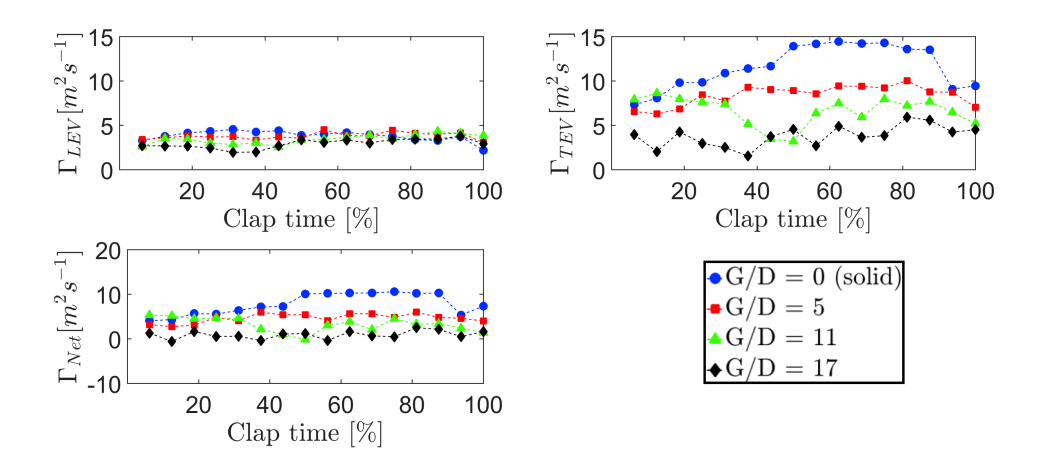


Figure 12. LEV, TEV and net circulation in clap.

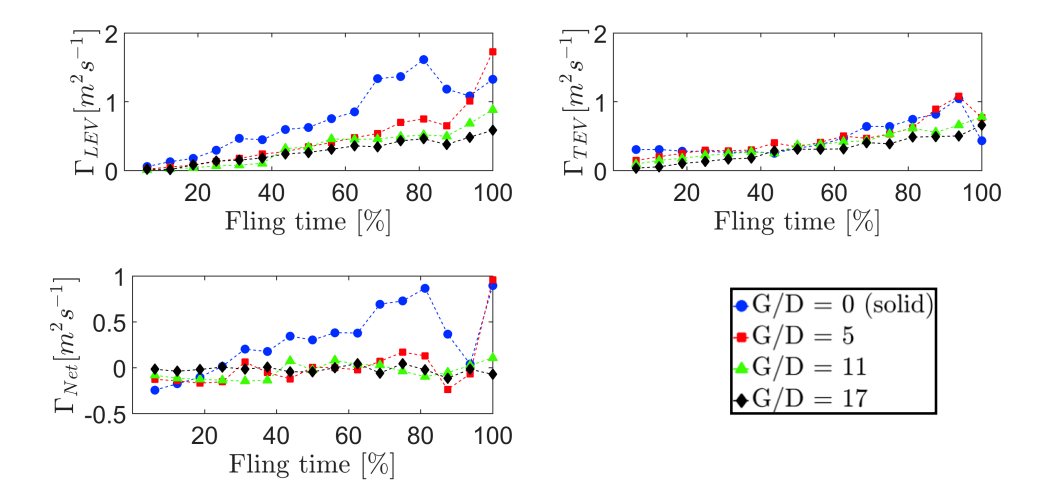


Figure 13. LEV, TEV and net circulation in fling.

the bristled wing model with G/D = 17 (not shown). We did not observe such small-scale vortices for bristled wing model with G/D = 5 (not shown). This could be due to the fact that the bristled wing model with G/D = 5 has lesser gaps between the bristles, causing the recirculating vortices around each bristle to diminish. In direct contrast to the observation of flow through bristles in fling, we did not observe the formation of any recirculating vortices for all the bristled wing models during clap (Figure 15).

# IV. Summary

In this study, we observed the following: (1) during wing-wing interaction, both lift and drag coefficients were lowered in the case of bristled wings when compared to those of solid wings across both clap and fling phases at the range of low Re tested in this study; (2) the reduction in  $C_D$  for bristled wing as compared to a solid wing was disproportionally larger when compared to reduction in  $C_L$  between bristled and solid wings during both clap and fling phases; (3) peak lift over peak drag  $(C_{L,max}/C_{D,max})$  was largest for bristled wings compared to solid wings across the entire range of Re from 5 to 15.

During wing-wing interaction, both aerodynamic forces  $(C_L, C_D)$  decrease with increase in G/D. The drop in peak lift force was not appreciable with increase in G/D during both clap and fling. Peak drag force decreased with increasing G/D, but not to the extent of drag reduction between solid and bristled wings. This shows that increase in G/D minimally impacts lift force generation in comparison to drag force.

The above results suggest that clap and fling interaction with bristled wings provides unique benefits over solid wings in terms of augmenting the overall aerodynamic efficiency of flapping flight.



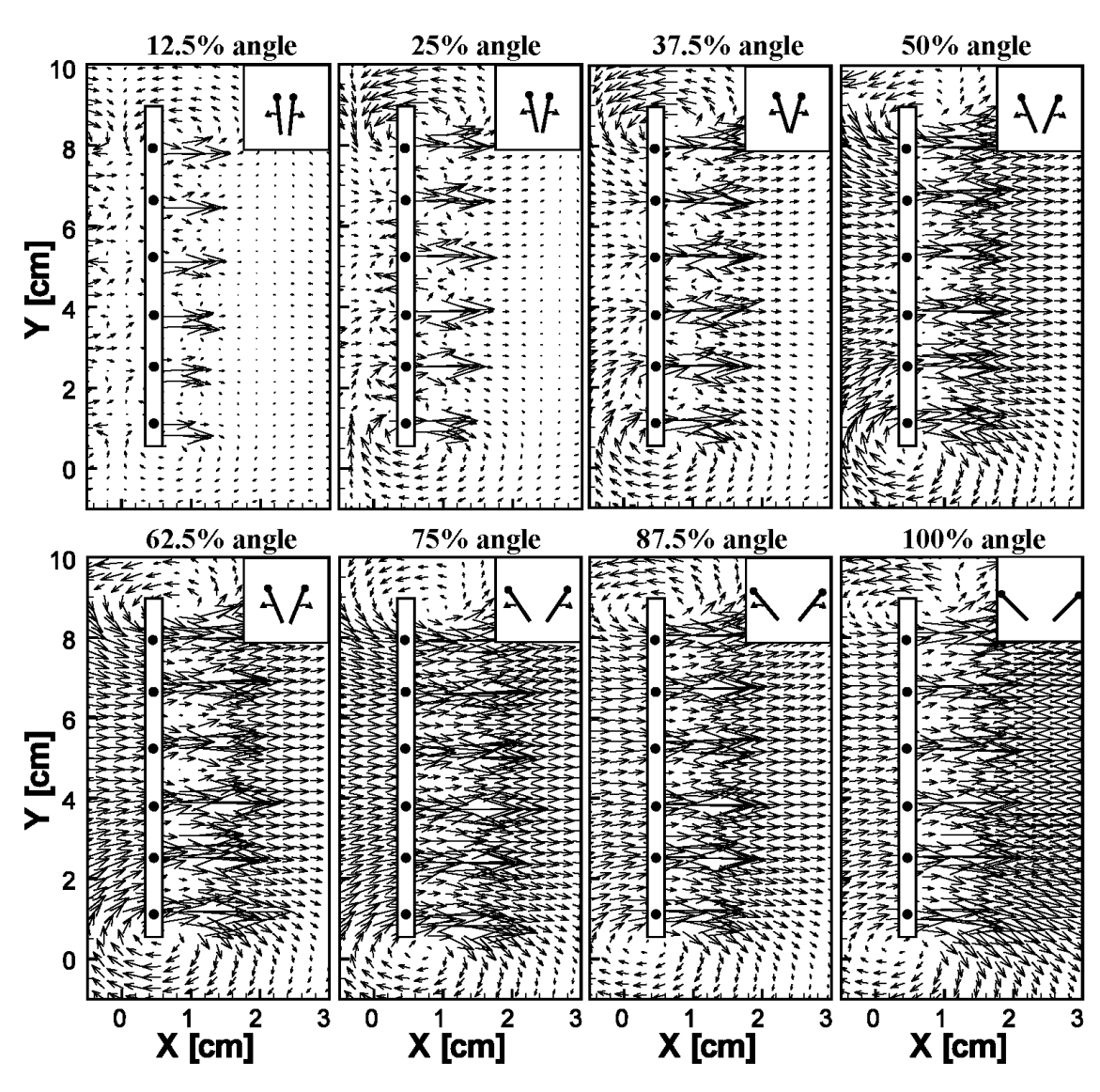


Figure 14. Velocity vector fields showing flow through the bristles during fling for a bristled wing model (G/D=11) at Re=10. Small-scale vortices form in between the bristles at 37.5% fling angle and eventually dissipate at higher angles.



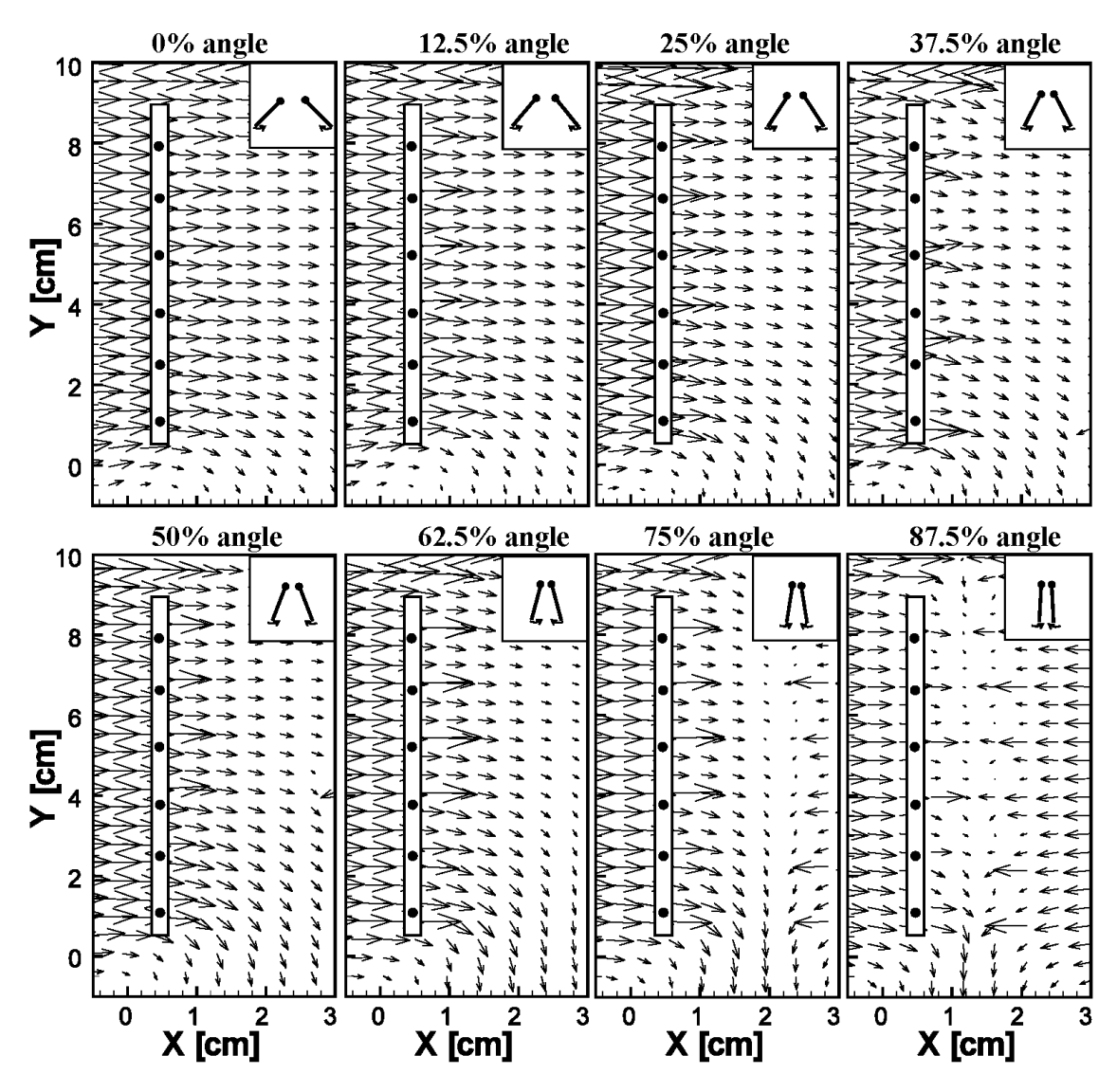


Figure 15. Velocity vector fields showing flow through the bristles during clap for a bristled wing model (G/D=11) at Re=10. Small-scale vortices in between the bristles are not observed in clap.

# V. Acknowledgements

The work presented in this paper was made possible by the support of the National Science Foundation grant CBET 1512071 awarded to Arvind Santhanakrishnan.

# VI. References

L. A. Miller and C. S. Peskin, "A computational fluid dynamics study of 'clap and fling' in the smallest insects," J. Exp. Biol., vol. 208, pp. 195-212, 2005.

A. Santhanakrishnan, A. K. Robinson, S. Jones, A. A. Low, S. Gadi, T. L. Hedrick and L. A. Miller, "Clap and fling mechanism with interacting porous wings in tiny insect flight," J. Exp. Biol., vol. 217, no. 21, pp. 3898-3909, 2014.

- S. K. Jones, Y. J. J. Yun, T. L. Hedrick, B. E. Griffith, and L. A. Miller, "Bristles reduce the force required to 'fling' wings apart in the smallest insects," J. Exp. Biol., vol. 219, no. 23, pp. 3759-3772, 2016.
- T. Weis-Fogh, "Unusual mechanisms for the generation of lift in flying animals," Sci. Am., vol. 233, pp. 81-87, 1975.
- J. Zhou, R. J. Adrian, S.Balachandar, and T. M. Kendall, "Mechanisms for generating coherent packets of hairpin vortices in channel flow," J. Fluid Mech., vol. 387, pp. 353-396, 1999.
- C. P. Ellington, "Non-Steady-State Aerodynamics of the Flight of Encarsia Formosa," Swimming and Flying in Nature. Springer, Boston, MA, 1975.
  - S. P. Sane, "The aerodynamics of insect flight," J. Exp. Biol., vol. 206, pp. 4191–4208, 2003.
- C. P. Ellington, "Wing mechanics and take-off preparation of Thrips (Thysanoptera)," J. Exp. Biol., vol. 85, pp. 129-136, 1980.
- J. M. Birch, W. B. Dickson, and M. H. Dickinson, "Force production and flow structure of the leading edge vortex on flapping wings at high and low Reynolds numbers," J. Exp. Biol., vol. 207, no. 7, pp. 1063–1072, 2004.
- G. R. Spedding and T. Maxworthy, "The generation of circulation and lift in a rigid two-dimensional fling," J. Fluid Mech., vol. 165, no. 1, p. 247, 1986.
- C. P. Ellington, "The Aerodynamics of Hovering Insect Flight . IV . Aerodynamic Mechanisms," vol. 305, no. 1122, pp. 79–113, 1984.
- S. Sunada, H. Takashima, T. Hattori, K. Yasuda, and K. Kawachi, "Fluid-dynamic characteristics of a bristled wing," J. Exp. Biol., vol. 205, pp. 2737–2744, 2002.
- C.R. Rodriguez-Saona, S. Polavarapu, J.D. Barry, D. Polk, R. Jornsten, P.V. Oudemans, O.E. Liburd, "Color preference, seasonality, spatial distribution and species composition of thrips (Thysanoptera: Thripidae) in northern highbush blueberries," Crop Protection, vol. 29, pp. 1331–1340, 2010.
- L. A. Mound and Y. F. Ng, "An illustrated key to the genera of Thripinae (Thysanoptera) from South East Asia," Zootaxa, vol. 2265, pp. 27–47, 2009.